Localization of electronic states in hybrid nanoribbons in the nonperturbative regime

Thomas Luu [1,*] Ulf-G. Meißner [2,1,3,†] and Lado Razmadze [1,2,‡]

[1]*Institute for Advanced Simulation (IAS-4), and Jülich Center for Hadron Physics, Forschungszentrum Jülich, 52425 Jülich, Germany*

[2]*Helmholtz-Institut für Strahlen- und Kernphysik and Bethe Center for Theoretical Physics, Rheinische Friedrich-Wilhelms-Universität Bonn, 53115 Bonn, Germany*

[3]*Tbilisi State University, 0186 Tbilisi, Georgia*

(Received 25 May 2022; revised 17 October 2022; accepted 8 November 2022; published 23 November 2022)

We investigate the localization of low-energy single quasiparticle states in 7/9- and 13/15-hybrid nanoribbon systems in the presence of strong interactions and within a finite volume. We consider two scenarios, the first being the Hubbard model at half filling, and perform quantum Monte Carlo simulations for a range U that includes the strongly correlated regime. In the second case, we add a nearest-neighbor superconducting pairing Δ and take the symmetric line limit, where Δ is equal in magnitude to the hopping parameter t. In this limit, the quasiparticle spectrum and wave functions can be directly solved for general on-site interaction U. In both cases, we extract the site-dependent quasiparticle wave-function densities and demonstrate that localization persists in these nonperturbative regimes under particular scenarios. Our findings suggest that such localization under the presence of interactions and within a finite volume is a generic feature of hybrid nanoribbons composed of topologically distinct regions.

DOI: 10.1103/PhysRevB.106.195422

I. INTRODUCTION

Recently, it was shown that localized, low-energy states can occur at the junction of two nanoribbons that are topologically distinct [1]. The presence of such symmetry-protected topological (SPT) localized states depends on their junction geometry and topological invariance. The ability to engineer such hybrid ribbons [2,3] has spurred research into the use of these systems for manufacturing quantum dots [4], potentially leading the way to novel, advanced electronic devices and an avenue for obtaining fault-tolerant quantum computing.

The existence of localized edge states has been widely explored in, for example, zigzag nanoribbons [5] where, depending on the the presence of interactions and/or disorder, the ribbon can change from a topological insulator to a trivial or Mott insulator [6,7]. On the other hand, the hybrid armchair configurations we consider here are less studied despite their promise as an interesting nanoengineering candidate. In some sense, they represent the next simplest ribbon geometry that can support localized states. As in the zigzag nanoribbon case, these localized states are manifest in the noninteracting, tight-binding scenario. However, SPT protection is only strictly enforced when both ribbons extend infinitely from their junction, as the topological invariants are calculated for infinite armchair graphene nanoribbons (AGNRs). The system has a very small energy gap compared to the hopping parameter. Though Ref. [1] demonstrated the stability of such states under perturbation, the extent to which these SPT states remain low energy, as well as localized, in the strongly interacting regime is an open question, especially since any practical implementation of these hybrid systems will be finite in extent or perhaps in a repeating lattice.

In this paper, we address the question of finite volume directly by investigating the *periodic* 7/9- and 13/15-hybrid nanoribbons in two distinct nonperturbative regimes. The term *finite volume* here refers to the fact that the distance between each junction is finite in length due to the systems' periodicity. The first nonperturbative regime we consider is the standard Hubbard model applied to these systems at the electrically neutral, half-filling case. Here we perform quantum Monte Carlo (QMC) simulations for various values of the on-site coupling U that include the strongly interacting regime. In the second regime, we consider the so-called symmetric line limit [6,8], where we introduce a nearest-neighbor superconducting pairing term Δ to the Hubbard model but with equal weight as the hopping term t. In this limit, the single-particle spectrum and wave functions, when expressed in a Majorana basis, can be determined for any value of the Hubbard on-site interaction U. In both cases, we observe that the energy of the localized state depends strongly on the coupling U. However, it still remains the lowest energy state of the system. Further, we find that under certain conditions the localization of these states at the junction persists.

Our paper is organized as follows. In Sec. II, we describe our 7/9 and 13/15 hybrid lattice geometries. We explicitly show the 7/9 spectrum in the tight-binding, or noninteracting, limit; the 13/15 spectrum is very similar in nature. We then introduce a Hubbard on-site interaction U in Sec. III and show results of our QMC simulations for select values of U. In Sec. IV, we consider the symmetric line limit by adding a nearest-neighbor superconducting term Δ of equal

*t.luu@fz-juelich.de
†meissner@hiskp.uni-bonn.de
‡s6larazm@uni-bonn.de

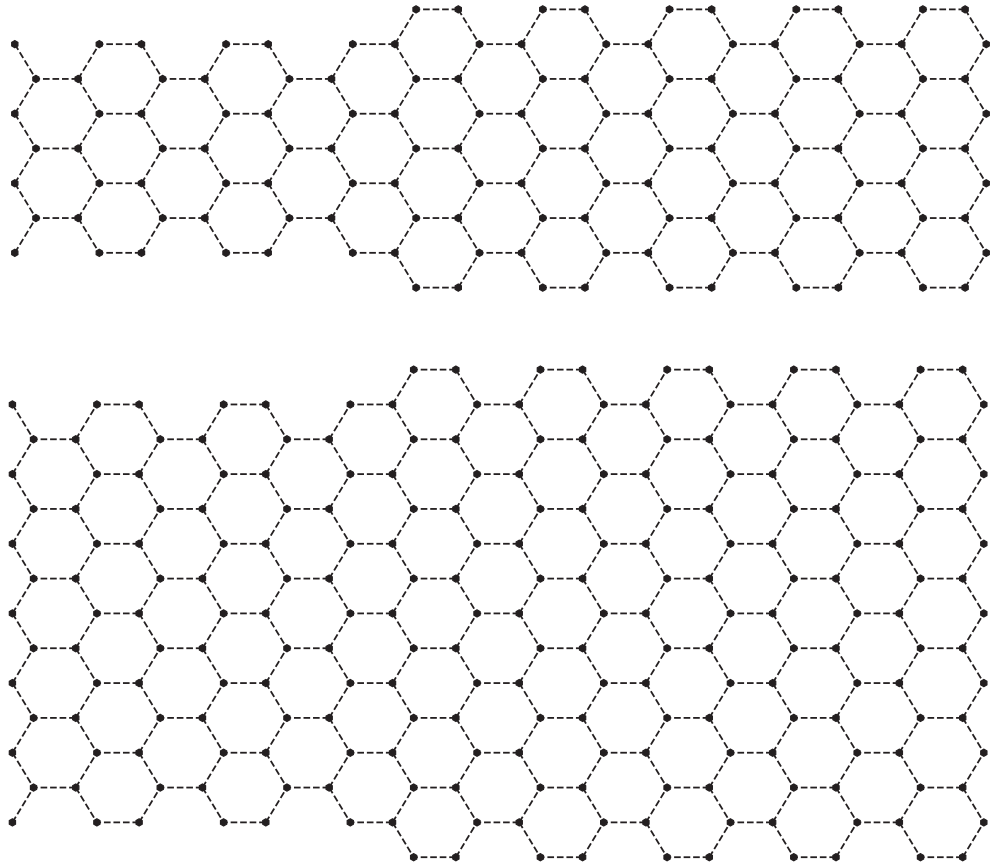

FIG. 1. Single unit cell of the 7/9 (top) and 13/15 (bottom) hybrid systems considered in this paper. The widths are set by the 7 (13) and 9 (15) armchair nanoribbon parts, while the lengths have six hexagons and ten hexagons for the 7 (13) and 9 (15) parts, respectively. Periodic boundary conditions are employed at the ends.

magnitude to the hopping term. We demonstrate how this system can be solved directly for any value of U and show the dependence of the energy and wave function of the localized state on U for the 7/9 case. These localized states on opposing sublattices, or chiralities, have a potential connection to domain-wall fermions formulated in lattice gauge theories in $4+1$ dimensions [9,10]. We comment on this potential connection in Sec. V. We recapitulate in Sec. VI.

II. GEOMETRY OF THE PERIODIC HYBRID NANORIBBON

Unit cells in such AGNRs are defined by their terminations, i.e., shapes of their edges. In Ref. [1], four distinct types of unit cells were defined. Based on inversion and mirror symmetries, as well as the width of ribbons, it has been shown that such systems have an associated conserved quantity, the so-called Z_2 topological invariant, that can take the values 0 or 1. The interface of two materials with distinct topological invariants can support surface modes [11]. Since the existence of these modes depend solely on the topological factors, they should remain even under the presence of interactions, given that these interactions do not change the invariants themselves. The two examples used in this paper are the 7/9- and 13/15-hybrid nanoribbons, where parts of the ribbons with lesser width have topological invariant $Z_2 = 0$, while the parts with greater width have invariant $Z_2 = 1$ [1]. The 7/9 system has recently been experimentally engineered [2,3].

Both systems are shown in Fig. 1. In both cases, the figure depicts a single unit cell. The 7/9 (13/15) has $N = 132$ (228) total lattice sites and is composed of six hexagonal units lengthwise for the lesser AGNR part, and ten hexagons lengthwise for the greater AGNR part. In terms of the lattice spacing a between sites, the entire length of the unit cell is $L = 24a$. The system is bipartite, meaning we can divide the lattice into two independent sublattices, which we label one as consisting of A sites, and the other B sites. We apply periodic boundary conditions at the ends so the unit cell shown in Fig. 1 repeats itself.

Under the tight-binding approximation or, equivalently, the noninteracting limit, we have

$$H_0 = -t \sum_{\langle i,j\rangle,\sigma} a^\dagger_{i\sigma} a_{j\sigma} + \text{H.c.}, \tag{1}$$

where t is the hopping parameter[1], $a^\dagger_j$ (a_j) is the fermionic creation (annihilation) operator at lattice site j, σ the spin, H.c. stands for Hermitian conjugate, and the sum is over all nearest neighbors $\langle i, j\rangle$. As the Hamiltonian is quadratic in

[1]For the tight-binding description of graphene, $t \sim 2.7$ eV [12].

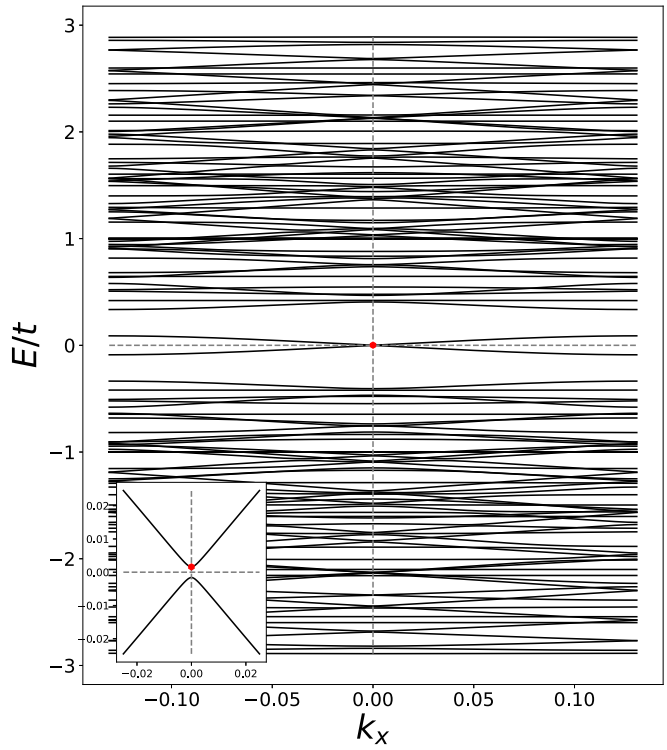

FIG. 2. Noninteracting dispersion of the 7/9 hybrid ribbon. The inset shows the avoided level crossing near the Fermi surface at $k_x = 0$. k_x is expressed in units of the inverse length L^{-1} with $L = 24a$ being the unit cell length and a the lattice spacing. The dispersion for the 13/15 system has more upper and lower bands but is qualitatively similar in structure.

the number of creation and annihilation operators, the single particle dispersion as a function of longitudinal momentum k_x can be easily determined in this limit, which we show for the 7/9 case in Fig. 2. Note that the dispersion is the same for both spins. The number of bands shown in Fig. 2 corresponds to the number of lattice sites in the unit cell (132 for the 7/9 case). Aside from having more upper and lower bands due to the larger number of unit cell lattice sites, the dispersion for the 13/15 case is qualitatively similar to the 7/9 case. Of particular interest is the point at $k_x = 0$ where there seems to be an apparent level crossing at $E/t = 0$, denoted as a red point in the main plot in Fig. 2. In fact, upon closer inspection, as shown in the inset of Fig. 2, there is *no* level crossing at this point since it consists of two states with energies $E/t = \pm 0.0015996$. For the 13/15 case, there is also an avoided level-crossing and the corresponding energies are $E/t = \pm 0.0090408$. In Fig. 3, we show the wave-function densities, $\rho(x) = |\psi(x)|^2$, for each lattice site x on an extended hybrid system for these states on these two geometries. These densities are the same for either positive or negative energy solutions. The localization of the states at the junctions is apparent in this figure. Further, the localization is confined to specific sublattices denoted by the red and blue colors in Fig. 3, and alternates between the different junctions.

In what follows, we assume that the system is electrically neutral and thus half-filled, meaning that all negative energy states are occupied. The Fermi surface of the system then corresponds to zero energy. We thus concentrate on the lowest *unoccupied* single-particle state. In the noninteracting case, this corresponds to the state denoted by the red dot in the inset of Fig. 2. In the remainder of the paper, we loosely refer to this state as the localized state, though it remains to be seen if the state remains localized in the presence of interactions and within a finite volume.

III. QMC CALCULATIONS OF THE HUBBARD MODEL

We now include a Hubbard on-site interaction,

$$H = -t \sum_{\langle i,j\rangle,\sigma} (a^\dagger_{i\sigma} a_{j\sigma} + \text{H.c.}) + U \sum_x \left(n_{x\uparrow} - \frac{1}{2}\right)\left(n_{x\downarrow} - \frac{1}{2}\right), \quad (2)$$

where $n_{x\uparrow} = a^\dagger_{x\uparrow} a_{x\uparrow}$ is the number operator for spin up fermions at site x and similarly for spin-down fermions. The form of the interaction ensures that the system remains at half filling for any value of U. In what follows, we assume that all stated values of U and β are expressed in units of the hopping parameter t, i.e., $U = U/t$, $\beta = t\beta$. All derived quantities, such as energies, are then expressed in units of t. Without loss of generality, this is equivalent to setting $t = 1$ in Eq. (2) for our simulations.

Note that the on-site interaction is quartic in the number of creation and annihilation operators, and therefore no direct diagonalizaton is possible. Therefore, we use QMC

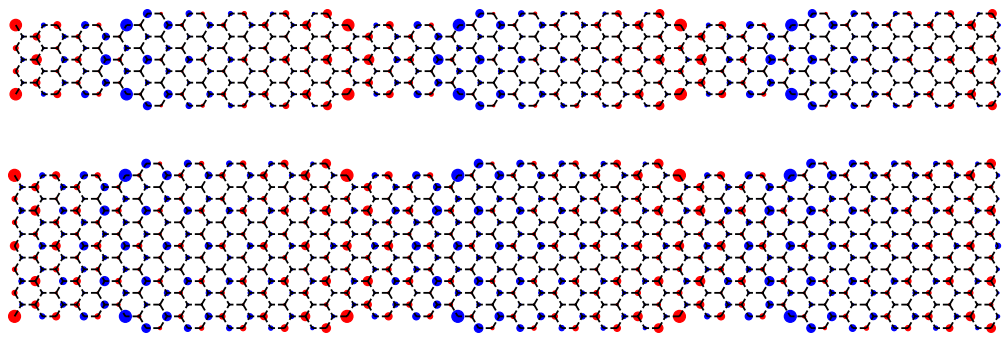

FIG. 3. Noninteracting single-particle wave-function densities for the 7/9 (above) and 13/15 (below) hybrid ribbons. The 7/9 and 13/15 configurations have noninteracting energies $E/t = 0.0015996$ and 0.0090408, respectively. The size of the circles is proportional to the density and the color denotes the two sublattices, red = A sites, blue = B sites.

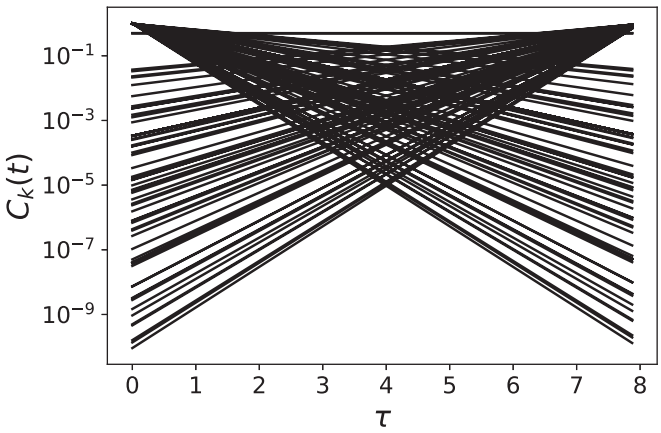

FIG. 4. All noninteracting correlators at $k_x = 0$ for the 7/9 system.

simulations to investigate the hybrid systems for values of the on-site interaction U corresponding to the strongly coupled regime. Our formalism for performing QMC simulations of low-dimensional Hubbard systems has been described in detail in Refs. [13–15]. Here we just point out some salient features pertinent to this paper.

To extract the quasiparticle energies, we calculate momentum correlators as a function of time,

$$C_k(\tau) \equiv \langle a_k(\tau) a_k^\dagger(0)\rangle = \frac{1}{Z}\,\mathrm{Tr}\,[a_k(\tau) a_k^\dagger(0) e^{-\beta H}], \quad (3)$$

where β represents an inverse temperature and $k = (k_x, \kappa)$ is a momentum index corresponding to the state. The time $\tau \in [0, \beta)$, and in our simulations we discretize this variable into N_t time slices. We use $N_t = 64,\ 80$ and 96 in our simulations with $\beta = 8,\ 10$, and 12, respectively, for the 7/9 system. For the 13/15 system, we only investigate with $(N_t, \beta) = (64, 8)$. The variable κ is an index corresponding to one of the possible $N = 132$ (228) states of the 7/9 (13/15) system for a given k_x. We choose κ to correspond to the state with the lowest possible positive energy. Figure 4 shows all $k_x = 0$ correlators at the noninteracting $U = 0$ case and $\beta = 8$ for the 7/9 system. A spectral decomposition of the expression in Eq. (3), as done in Appendix, shows that these correlators have an exponential dependence in time, $\sim e^{-E_k \tau}$, where their arguments correspond to the noninteracting energies of the system at $k_x = 0$. These energies correspond to both the positive and negative points that occur at $k_x = 0$ in Fig. 2. In the presence of interactions $U \neq 0$, and within a finite inverse temperature β, the correlators will have a more complicated dependence on τ due to thermal contamination with excited states and backward-propagating states. However, these effects are usually fleeting since the dependence on the excited states is exponentially suppressed. Therefore, as long as $\tau \gg 1$ but $\tau < \beta$, the correlators will recover an exponential dependence but now with fully interacting energies in their arguments. One can thus extract the fully interacting energies by analyzing the exponential behavior of the correlators in this regime. We stress that the correlator in Eq. (3) and the energy E_k dictating its exponential decay are not related to any response of the system due to some external probe. The energy E_k represents the fully interacting single-particle eigenenergy of the Hamiltonian given in Eq. (2).[2]

Special care must be taken when dealing with correlators that represent states with very small energies, $E\beta \ll 1$, as is the case in our situation. Here the backward-propagating states can provide a nearly equally important contribution to the correlator, essentially making the correlator symmetric about the $\tau = \beta/2$ point. The left panel of Fig. 5 shows examples of the dependence of the correlators for the localized state as a function of U. It is indeed the case that these low-energy correlators cannot be described by a single exponential. We now describe how we extract energies from these correlators.

A. Energy of the localized states

To extract the energies from these correlators, we first take advantage of the particle-hole symmetry of our problem that states that for any energy solution E_k, there is a corresponding solution with opposite sign, $-E_k$. This is also evident from our correlators, where for each correlator that falls off in time as $C_k^-(\tau) \sim e^{-E_k \tau}$, there is a growing correlator, corresponding to the energy with opposite sign, of the form $C_k^+(\tau) \sim e^{E_k(\tau-\beta)}$. We average these two correlators,

$$C_k^{\mathrm{sym}}(\tau) = \tfrac{1}{2}(C_k^-(\tau) + C_k^+(\tau)), \quad (4)$$

to effectively make a cosh function of the form $\cosh[E_k(\tau - \beta/2)]$ in the regions $\tau \gg 1$ and $\tau < \beta$.

As a visual aid to estimating the energies of these correlators, we calculate the so-called effective mass $m_{\mathrm{eff}}(\tau)$,

$$m_{\mathrm{eff}}(\tau) = \frac{1}{\delta}\cosh^{-1}\left(\frac{C_k^{\mathrm{sym}}(\tau-\delta) + C_k^{\mathrm{sym}}(\tau+\delta)}{2C_k^{\mathrm{sym}}(\tau)}\right), \quad (5)$$

where δ is some free parameter. If $C_k^{\mathrm{sym}}(\tau)$ were exactly a cosh function, then $m_{\mathrm{eff}}(\tau) = E_k$ for all τ. As the cosh behavior is only valid for $1 \ll t \ll \beta$, we expect that the effective mass to flatten out around the region $\tau = \beta/2$. The right panel of Fig. 5 shows our extracted effective masses for the localized state using $\delta = 4\beta/N_t$. As expected, the region around $\tau = \beta/2$ is flat and corresponds to the interacting energy E_k/t. We stress, however, that these effective masses are only used as a visual aid for estimating the energies.

To actually obtain the energies, we instead fit directly the correlator $C_k^{\mathrm{sym}}(\tau)$. We show our extracted energies for values of $U \in [1, 2, 3, 4]$ and $\beta \in [8, 10, 12]$ in Fig. 6. Our fits are performed within a finite window around the $\tau = \beta/2$ point and are done under the bootstrap procedure to obtain uncertainties. Looking at Fig. 6, we see a growing dependence on the energy of the localized state as U increases. We attribute this dependence to the finite volume of the system, both spatially and temporally, since within such an environment the state is no longer protected by SPT. Still, in all cases we examined we found that the energy of the localized state remained the lowest, despite its apparent dependence on U.

[2]In practice, the calculation of the correlator in Eq. (3) requires calculating the inverse of the so-called fermion matrix M and then analyzing its time dependence. More details of this method are provided, for example, in Refs. [14,19].

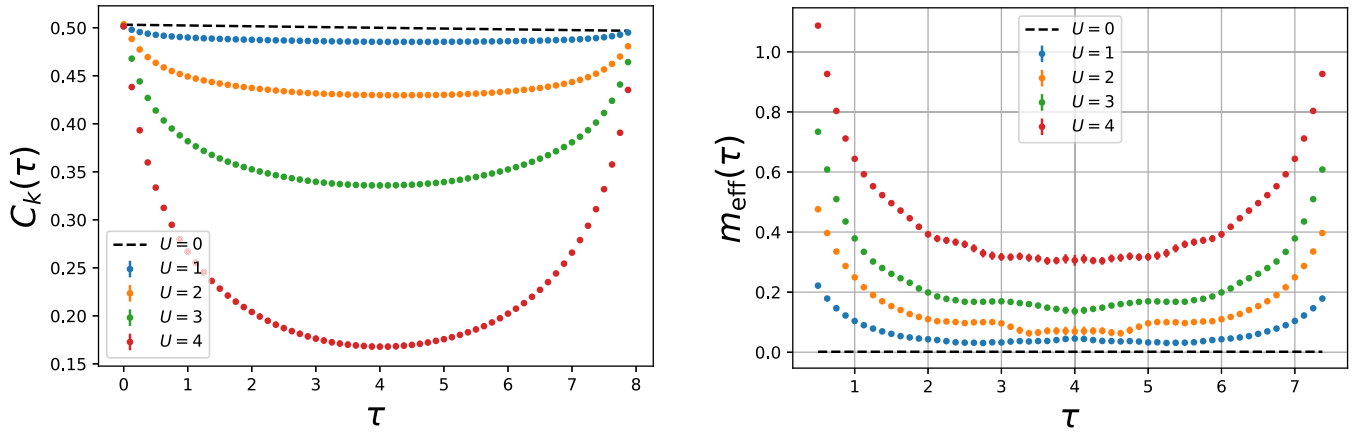

FIG. 5. Dependence of correlators for the lowest energy localized state (left) and its corresponding effective masses (right) as defined in Eq. (5). In both cases, the black dashed line corresponds to the noninteracting result.

B. Wave-function densities of the localized state

We can also extract the site-dependent densities of the states in our QMC simulations, which in turn allow us to demonstrate localization of the states visually. A detailed explanation of our calculation is given in the Appendix, and we provide only a cursory description here.

Instead of the momentum correlators calculated in Eq. (3), we instead consider the half-momentum, half-spatial correlators:

$$C_k(x,\tau) \equiv \langle a_x(\tau) a_k^\dagger(0)\rangle = \frac{1}{Z}\,\mathrm{Tr}\,[a_x(\tau) a_k^\dagger(0) e^{-\beta H}]. \quad (6)$$

The effective density $\rho_k(x,\tau)$ for state k at each lattice site x is given by

$$\rho_k(x,\tau) \equiv \frac{|C_k(x,\tau)|^2}{\sum_y |C_k(y,\tau)|^2}. \quad (7)$$

where the sum in the denominator of the right-hand side is over all lattice sites in the unit cell. As was the case with the effective masses, we extract the densities by looking at the region around $\tau = \beta/2$ where the effective density is flat. We plot these densities for the localized state in Fig. 7 for different values of U for the 7/9 system. We find that the changes in the densities vary only slightly as a function of U and are practically indistinguishable in Fig. 7. We see similar behavior for the 13/15 system. In Fig. 8, we concentrate on a specific lattice site of the 7/9 system, the bottom and leftmost sites of the unit cell, and show how the density at this site varies as U increases. When $U = 0$, this site is one of four A sites that has a maximum probability for occupation compared to other A sites. With increasing U, this density diminishes but still remains the largest. We find a similar behavior with other high-density sites on both 7/9 and 13/15 systems. For sites with initially low probabilities at $U = 0$, their densities slightly grow with increasing U. However, the changes are too small to drastically change the general electron occupation profile. Thus, the localization of this state persists as U grows large, despite its growing energy.

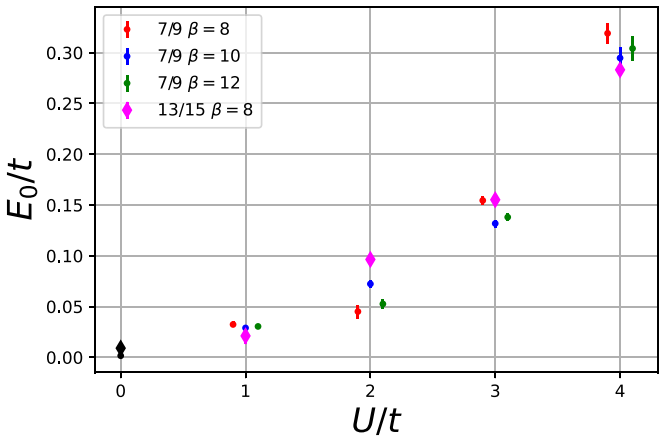

FIG. 6. Energy E_0 of the lowest state as a function of on-site interaction U obtained from QMC calculations for the 7/9 (dots) and 13/15 (diamonds) systems. The 7/9 simulations were performed with three different values of β, where $\beta = 8$ [Eq. (12)] results are slightly shifted to the left (right) on the x axis so as to make the points more easily differentiable. Only $\beta = 8$ was used for the 13/15 system. The black points at $U = 0$ are the noninteracting results.

Our results definitely show the strong dependence of the energy on U within a finite volume. The localization, however, is robust and persists in such environments. A more definitive QMC investigation of this state would require repeated calculations of this system with more values of β and number of time slices N_t, as well as more unit cells, allowing for extrapolations to zero temperature, to the continuum limit, and to the infinite volume (length), respectively. We are actively pursuing this line of research.

Still, the fact that these states remain localized for large values of U within such an extreme finite volume bodes well for their potential utilization in advanced electronics, which by construction are finite in extent.

IV. THE SYMMETRIC-LINE LIMIT

We now consider the inclusion of a nearest-neighbor superconducting pairing term Δ to the Hamiltonian:

$$H_0 = -\sum_{\langle i,j\rangle,\sigma} (t\, a_{i\sigma}^\dagger a_{j\sigma} + \Delta\, a_{i\sigma}^\dagger a_{j\sigma}^\dagger + \text{H.c.}) + U\sum_x \left(n_{x\uparrow} - \frac{1}{2}\right)\left(n_{x\downarrow} - \frac{1}{2}\right). \quad (8)$$

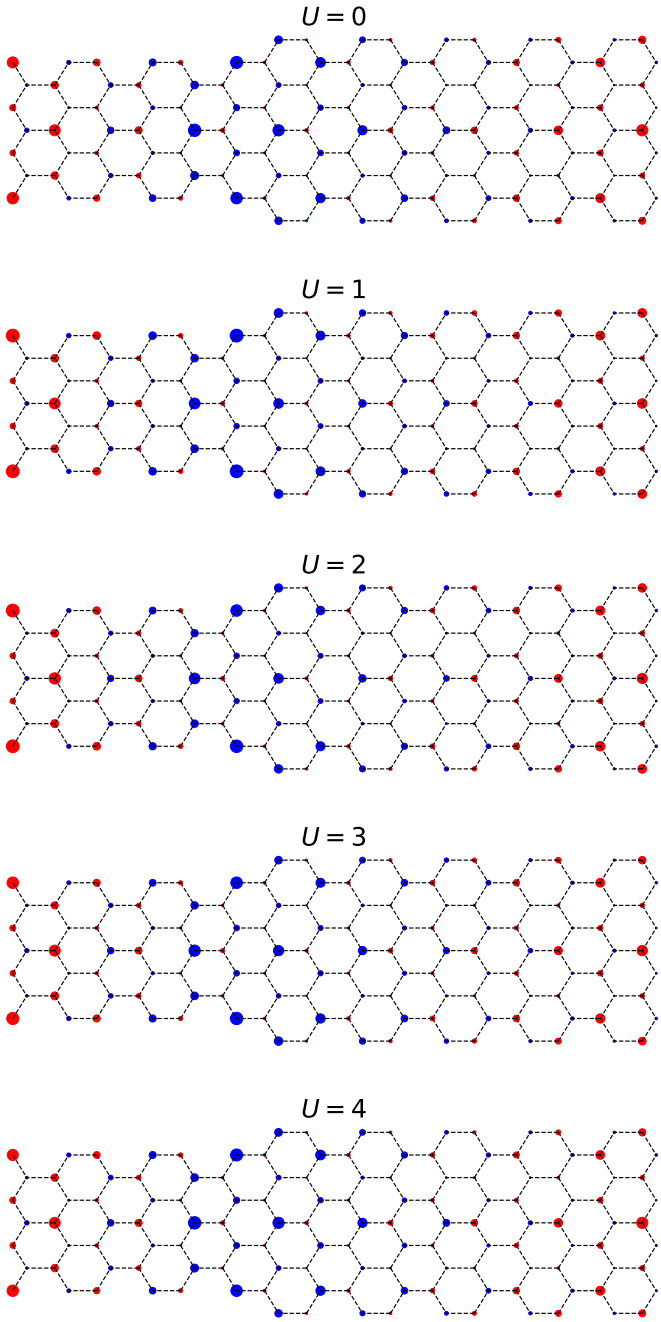

FIG. 7. Density profile of lowest $k_x = 0$ energy state for different values U, compared with the noninteracting case (i.e., $U = 0$).

The pairing term has the same symmetry properties as the hopping term and, in particular, the Hamiltonian remains invariant under time reversal. Therefore, the inclusion of this term does not change the topology of the system.

As described in Refs. [6–8], for example, when Δ has the same magnitude as the hopping parameter t, the on-site interaction term becomes quadratic in the number of creation and annihilation operators and therefore the spectrum of the system can be obtained by direct diagonalizations. We repeat the derivation for our system here. We follow the conventions introduced in Ref. [6].

Typically, one uses a Bogoliubov-Valatin transformation [16,17] in theories with pairing terms. However, in this case,

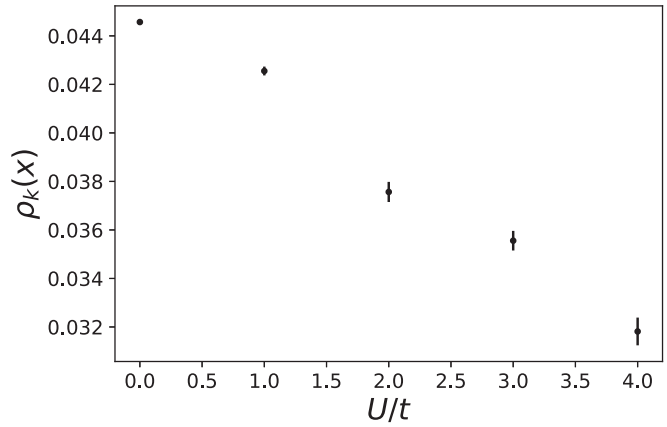

FIG. 8. Wave-function density $\rho_k(x)$ of the bottom- and leftmost lattice sites of our unit cell hybrid AGNR as a function of U.

with an eye toward the interacting on-site term, we instead perform a canonical transformation to a Majorana basis,

$$a_{i\sigma} = \eta_{i\sigma} + i\gamma_{i\sigma}, \quad a^\dagger_{i\sigma} = \eta_{i\sigma} - i\gamma_{i\sigma}, \quad a_{j\sigma} = \gamma_{j\sigma} + i\eta_{j\sigma},$$
$$a^\dagger_{j\sigma} = \gamma_{j\sigma} - i\eta_{j\sigma}, \tag{9}$$

where $i \in A$ sites and $j \in B$ sites. The Hamiltonian in Eq. (8) then becomes

$$H = -2i \sum_{\langle i,j\rangle\sigma} [(\Delta + t)\gamma_{i\sigma}\gamma_{j\sigma} + (\Delta - t)\eta_{i\sigma}\eta_{j\sigma}]$$
$$- U \sum_{x\in A\&B} (2i\eta_{x\uparrow}\eta_{x\downarrow})(2i\gamma_{x\uparrow}\gamma_{x\downarrow}). \tag{10}$$

We now take the symmetric line limit by setting $\Delta = t$, thereby eliminating the η Majorana fermions from the kinetic energy of the Hamiltonian above:

$$H_{\rm sym} = -4it \sum_{\langle i,j\rangle\sigma} \gamma_{i\sigma}\gamma_{j\sigma} - U \sum_{x\in A\&B} (2i\eta_{x\uparrow}\eta_{x\downarrow})(2i\gamma_{x\uparrow}\gamma_{x\downarrow}). \tag{11}$$

Notice that the γ Majorana fermions have a kinetic term similar to the original tight-binding Hamiltonian of Eq. (1), but now with a hopping amplitude $4t$. Indeed, when $U = 0$ the dispersion for this system, when normalized by $4t$, is identical to the noninteracting dispersion shown in Fig. 2.

Now consider the site-dependent operator $\hat{d}_j \equiv 2i\eta_{j\uparrow}\eta_{j\downarrow}$. One has that $[H_{\rm sym}, \hat{d}_j] = 0 \ \forall \ j$. Therefore, within Eq. (11), the term $2i\eta_{x\uparrow}\eta_{x\downarrow}$ $(= \hat{d}_x)$ can be replaced, in general, by a complex number d_x (no hat symbol). As can be derived explicitly from Eqs. (9), the Majorana operators η have the property that $\eta^2 = 1/4$, which implies that $\hat{d}_x^2 = 1/4$ [20]. Thus we can make the following replacement $\hat{d}_x \to d_x = \pm 1/2$ in Eq. (11). This gives

$$H_{\rm sym} = -4it \sum_{\langle i,j\rangle\sigma} \gamma_{i\sigma}\gamma_{j\sigma} - 2iU \sum_{x\in A\&B} d_x(\gamma_{x\uparrow}\gamma_{x\downarrow}). \tag{12}$$

The equation above shows that in the symmetric line limit, the η Majorana fermions completely decouple from the theory. They provide a zero-energy topological flat band to the dispersion, independent of U, but as argued in Ref. [6] these states do not correspond to localized states.

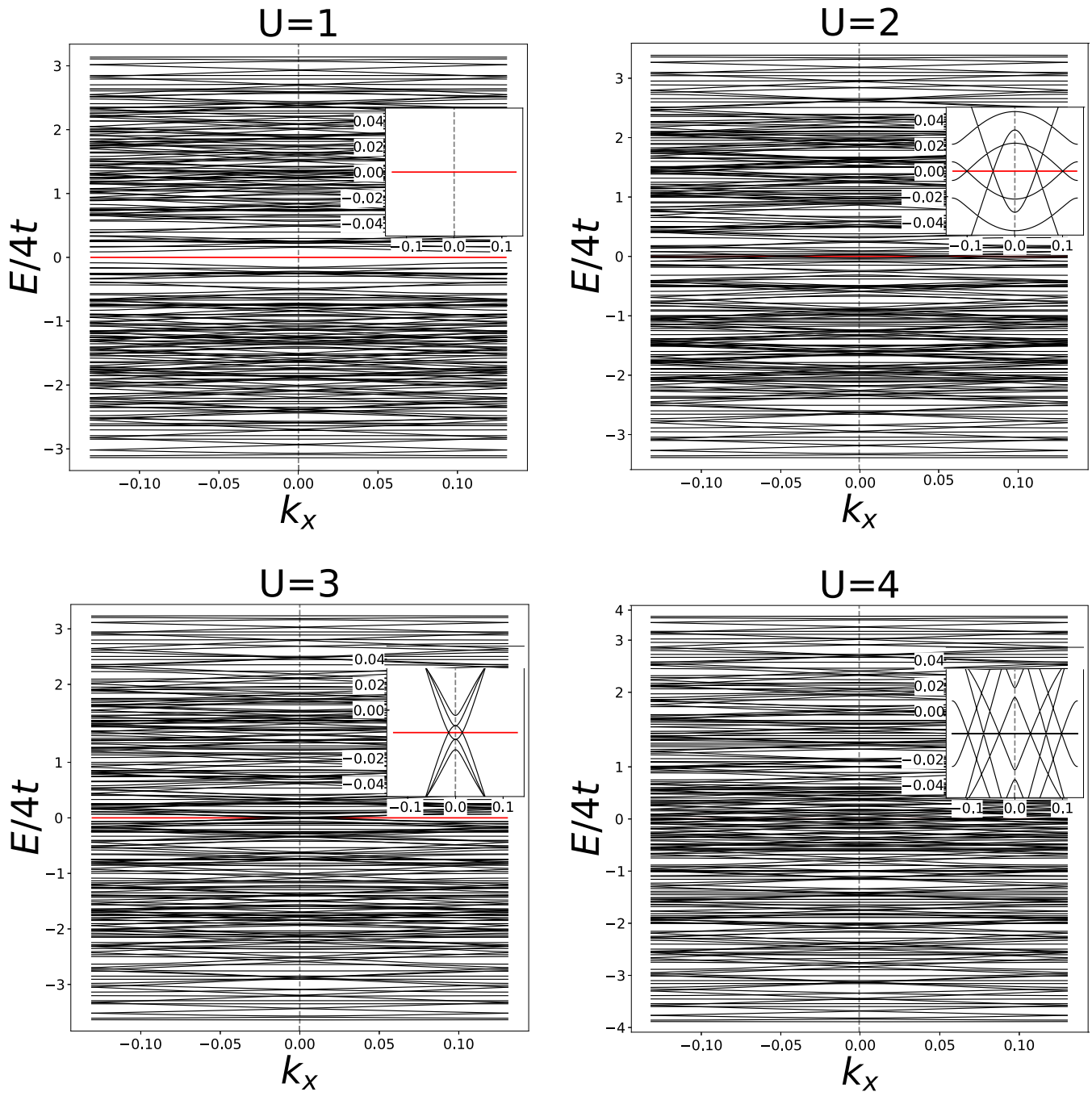

FIG. 9. Ferromagnetic dispersion in the symmetric line limit for different values of U. The red horizontal line is the flat band energy for the decoupled η Majorana fermions.

The Hamiltonian in Eq. (12) is quadratic in the Majorana operators and therefore can be directly diagonalized once the coefficients d_i are fixed. In principle, given N lattice sites, there are 2^N different possible combinations of d_i, all satisfying the flat band condition for the η Majorana fermions but providing a different spectrum for the γ Majorana fermions. We consider two uniform solutions in this paper, the first being the ferromagnetic solution with $d_i = 1/2\ \forall\ i$ and the other the antiferromagnetic case where $d_i = 1/2$ for $i \in A$ sites and $d_i = -1/2$ for $i \in B$ sites. Lastly, we consider a random configuration where $d_i = \pm 1/2$ is chosen randomly at each site i.

Since the discussion above applies to any bipartite lattice, we can directly use it on our systems. In our calculations, both 7/9 and 13/15 systems exhibit nearly identical qualitative results. To keep the presentation reasonable, we therefore only present results for the 7/9 system and comment on the 13/15 system when appropriate.

A. Ferromagnetic configuration

In this configuration, we choose $d_i = 1/2\ \forall\ i$. Our results are identical if we instead chose $d_i = -1/2\ \forall\ i$. We show the dispersion for this system for select values of U in Fig. 9. In

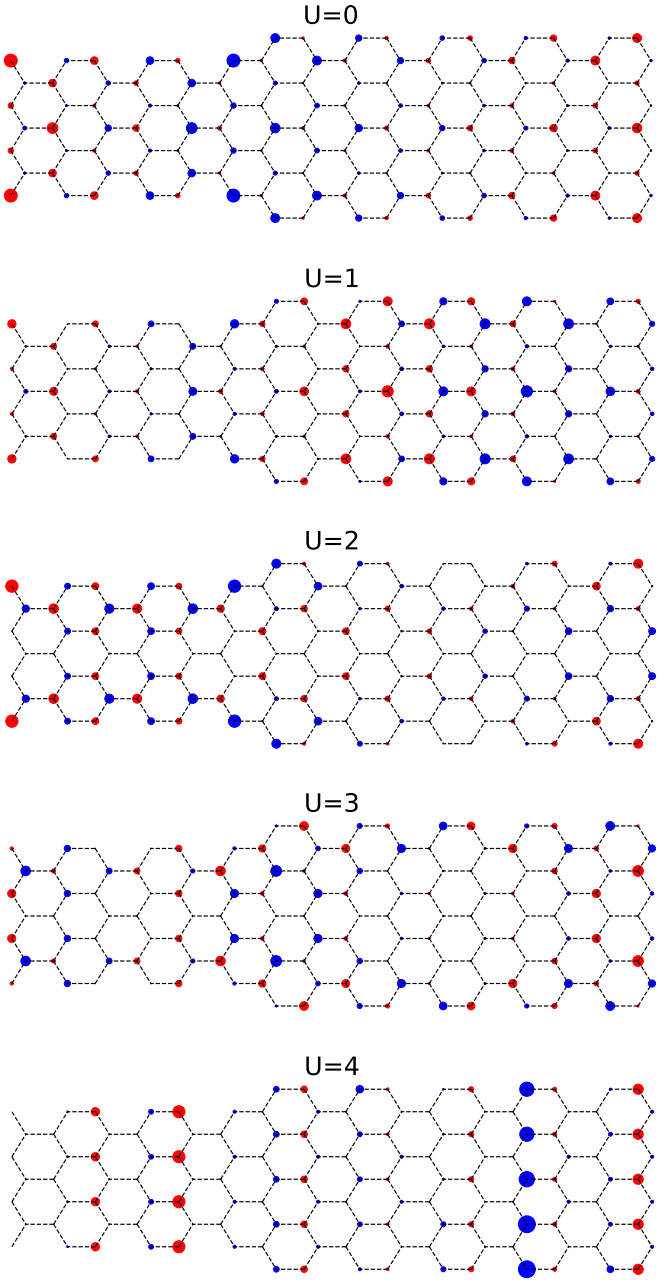

FIG. 10. Density profile of the lowest $k_x = 0$ energy state at the symmetric line limit for the ferromagnetic configuration for different values of U. The result is the same for either spins σ. Noninteracting case corresponds to $U = 0$.

general, the dispersion becomes quite dense and the separation between the lowest state and the next excited state diminishes as U is increased.

The wave function densities for the lowest energy state are shown in Fig. 10. We find that this configuration exhibits no localization at $k_x = 0$ for the large Us considered here, though we have confirmed that it is perturbatively recovered in the limit $U \to 0$.

Finally, the energy E_0 of the lowest state has a complicated dependence on the interaction term U, as shown in Fig. 11. This is due to the fact that we consider only the lowest positive energy level at $k_x = 0$. As U increases, the energy levels

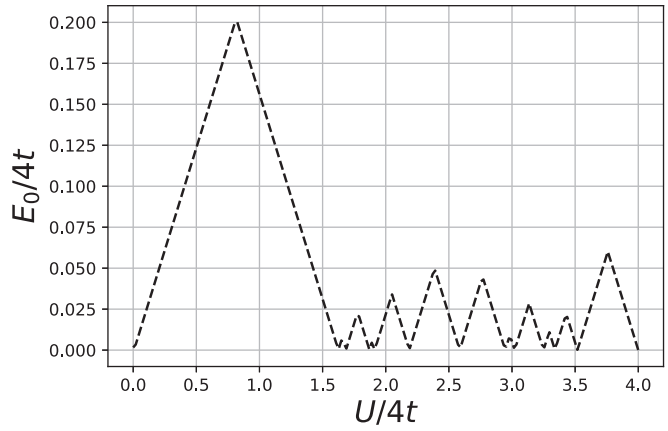

FIG. 11. Dependence of the lowest positive energy E_0 as a function of U in the ferromagnetic configuration.

from the upper and lower bands come together and eventually cross each other. Before each crossing, the minimal energy decreases and after a crossing it begins to increase again. Eventually, the lowest energy levels cross $E_0 = 0$ after which the next highest one takes its place.

B. Antiferromagnetic configuration

Figure 12 shows the dispersion of the hybrid ribbon at the symmetric line limit for select values of $U > 0$ in the antiferromagnetic configuration. Notice that the lowest positive energy increases with larger U and forms essentially a flat band solution. Numerically, we find a linear dependence of this energy on U, as shown in Fig. 13.

For all Us investigated, the wave-function densities of this state do not change and remain exactly the same as that of the noninteracting state shown in Fig. 3. Therefore, this state remains localized, despite its energy having a linear dependence on U. We conclude that the flat band that develops for $U > 0$ is robust and is unaffected by interactions. Unlike the ferromagnetic case, when we increase U the gap in the antiferromagnetic system increases linearly since no low-lying energy levels cross each other and therefore no complicated U dependence is introduced.

C. Random configuration

To a certain extent, a random configuration of d_is is similar to the antiferromagnetic configuration in that such a configuration has no long-range order. Thus, one might expect that the dispersion in the random configuration is similar to the antiferromagnetic case. We find this to be true for values of U as large as $U \lesssim 2$.

To see this, we first show in Fig. 14 the dispersion for different values U using a single randomly sampled configuration in each case. Not surprisingly, the dispersions becoming progressively dense and chaotic with increasing U. To construct the accompanying wave-function densities, we calculate 100 random configurations for each value of U and average their wave-function densities, the results of which are shown in Fig. 15. In this case, the localization of the lowest state can be seen for $U = 1$ and $U = 2$. However, for larger

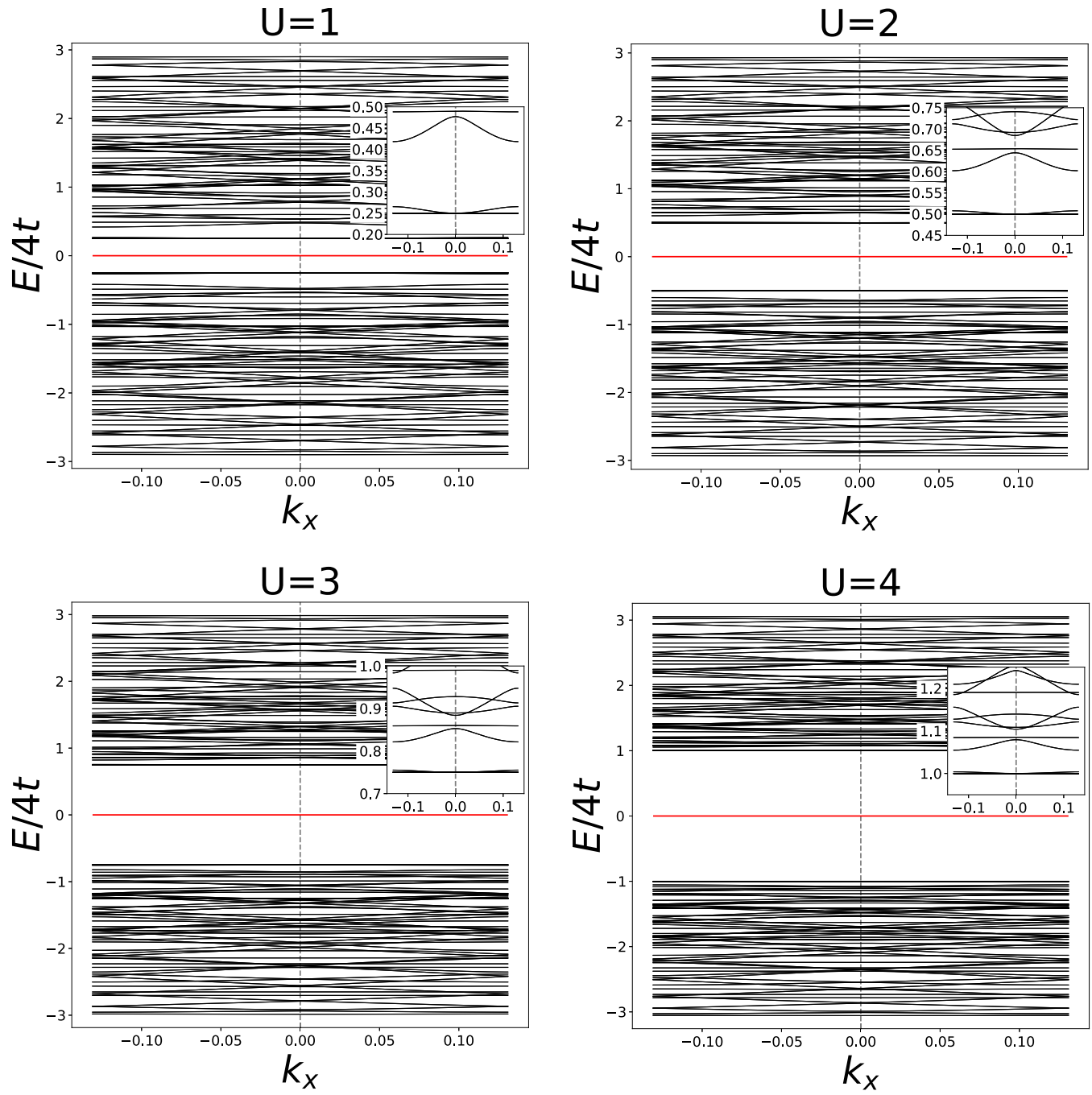

FIG. 12. Antiferromagnetic dispersion in the symmetric line limit for different values of U. The red horizontal line is the flat band energy for the decoupled η Majorana fermions.

U any analogies of the dispersion with the antiferromagnetic configuration is lost and localization is no longer present.

V. ANALOGY WITH DOMAIN-WALL FERMIONS

Domain-wall fermions were formulated originally by Kaplan [9] as a way to circumvent the so-called Nielsen-Ninomiya no-go theorem [18] in lattice gauge theory, which states that the number of left-handed chiral fermions ψ_L must equal the number of right-handed chiral fermions ψ_R in any discretized, local, Hermitian, and translationally invariant field theory. Kaplan's formulation of domain wall fermions introduced an extra bulk dimension on top of the four space-time dimensions, whereby a single fermion of one chirality was localized on the 4D spacetime manifold (the domain wall where all the relevant physics occurs) of the 5D space, and another fermion of opposite chirality was constrained on the opposite 4D domain wall. In this manner, lattice gauge calculations utilizing domain wall fermions could simulate, in principle, an odd number of fermions with specific chirality by concentrating on one of the 4D domain wall manifolds without violating the Nielsen-Ninomiya no-go theorem. Chiral

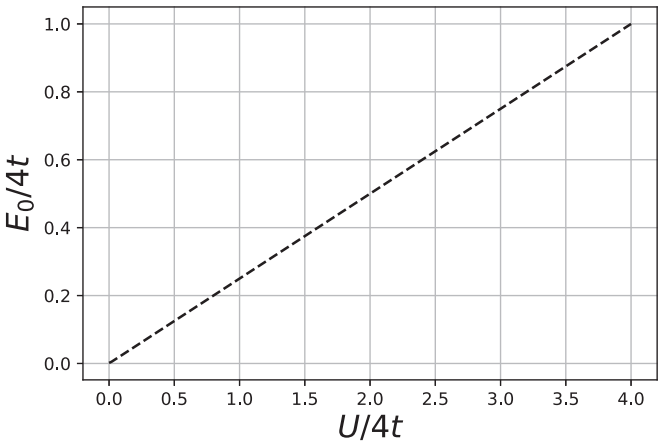

FIG. 13. Dependence of the lowest positive energy E_0 as a function of U in the antiferromagnetic configuration for 7/9 ribbon. The 13/15 system presents the same linear relation.

symmetry is still violated since the Ginsburg-Wilson equation remains nonzero in the bulk. This manifests itself as a small overlap of the fermion wave functions in the bulk, which in turn leads to a residual mass μ for each fermion that mixes their chiralities, $\mu(\bar{\psi}_L\psi_R + \bar{\psi}_R\psi_L)$. As the bulk direction is extended, the overlap reduces leading to a vanishingly small residual mass and therefore a vanishing chiral-symmetry violation. Kaplan's formulation is actually valid for any theory in $2n+1$ dimensions, where $2n$ represents the spacetime dimension and the extra dimension represents the bulk.

Chiral symmetry breaking has been discussed in the context of the 2D graphene hexagonal lattice (see, e.g., Refs. [21,22]). Here chiral symmetry manifests itself as a sublattice symmetry between the A and B sites and originates from an underlying time-reversal and charge-conjugate symmetry [23,24]. The low-energy Dirac modes of the system can be described by an effective relativistic field theory in $2+1$ dimensions. As argued in Ref. [21], the formation of a gap in these modes is equivalent to a staggered mass [25] for the fermions that breaks the sublattice symmetry.

In our ribbons, we may treat one of the spatial dimensions as the manifold, or junction, while the other remaining spatial dimension between the junctions as the bulk. If we concentrate on just the low-energy localized state of our system and describe it within some effective field theory, then the shift away from zero energy can also be represented as a staggered mass that presumably depends on the overlap of the wave functions of the two chiral edge states within the bulk, and thus should vanish as the bulk direction is extended. We find this to indeed be the case in the noninteracting limit, as we show in Fig. 16. Here we show the energy of the localized state for both 7/9 and 13/15 ribbons as we extend the bulk direction. There is a clear exponential decay in energy. Thus the localized states on opposite A/B sublattices at the junctions of the topologically distinct ribbons offer a potential physical realization of Kaplan's domain wall fermions, albeit in reduced dimensions. A formal description of these chiral states within an effective field theory context is something we are currently developing.

VI. CONCLUSIONS

Localized states at the junction of topologically distinct nanoribbons offer promising avenues in constructing advanced electronics and potentially provide a means for topological, fault-tolerant quantum computing. Central to this idea is the stability of such states not just to slight perturbations, but to large electron correlation effects. In principle, SPT provides this stability, but only in the limit of infinitely long ribbons where SPT invariance is manifest. In a finite volume, this protection is not guaranteed and, as such, the stability of such states comes into question when electron correlations become large.

In this paper, we investigated the stability of the (nearly) zero-mode localized states in finite 7/9 and 13/15 hybrid nanoribbons with periodic boundary conditions under the influence of temperature and electron-electron interactions. We investigated two scenarios, one where we considered just the Hubbard model at half filling and performed QMC simulations for a range of U that included the strongly interacting regime. We then introduced to the Hubbard model a nearest-neighbor superconducting term whose parameter was tuned to the so-called symmetric line limit. In this limit, when transforming to a Majorana basis, we could calculate the single-particle spectrum and wave functions exactly for any value of U. Provided that we concentrate on the antiferromagnetic configuration in the latter case, we found that in both cases the energy of the localized states increased with larger U, but remained the lowest energy state regardless. More importantly, we found that the localization of the states persisted at the junctions, indicating that this feature is robustly maintained in the strongly interacting, finite volume regime. Though by no means a proof, our observations of persistence of localization in both 7/9 and 13/15 hybrid geometries suggests that such effects are generic to other hybrid geometries that support localization, but this remains to be seen. These findings enhance the possibility of using these systems for manufacturing novel electronic devices which are inherently finite in volume.

ACKNOWLEDGMENTS

T.L. thanks Evan Berkowitz, Andrei Kryjevski, and Johann Ostmeyer for enlightening discussions related to this paper. This paper was supported in part by the Chinese Academy of Sciences (CAS) President's International Fellowship Initiative (PIFI) (Grant No. 2018DM0034) and Volkswagen Stiftung (Grant No. 93562).

APPENDIX: EXTRACTING SITE DENSITIES FROM QMC SIMULATIONS

To extract the amplitudes for each site, we first calculate site-dependent spatial correlators of the form

$$C_k(x,t) \equiv \langle a_x(t)a_k^\dagger(0)\rangle = \frac{1}{Z}\,\mathrm{Tr}\,[a_x(t)a_k^\dagger(0)e^{-\beta H}], \quad \text{(A1)}$$

where $Z = \mathrm{Tr}[e^{-\beta H}]$ and the trace is taken over the entire Fock space of the system. Here x refers to a particular site on the lattice and $k = (k_x, \kappa)$ is the momentum variable that corresponds to the state that we are interested in. The creation

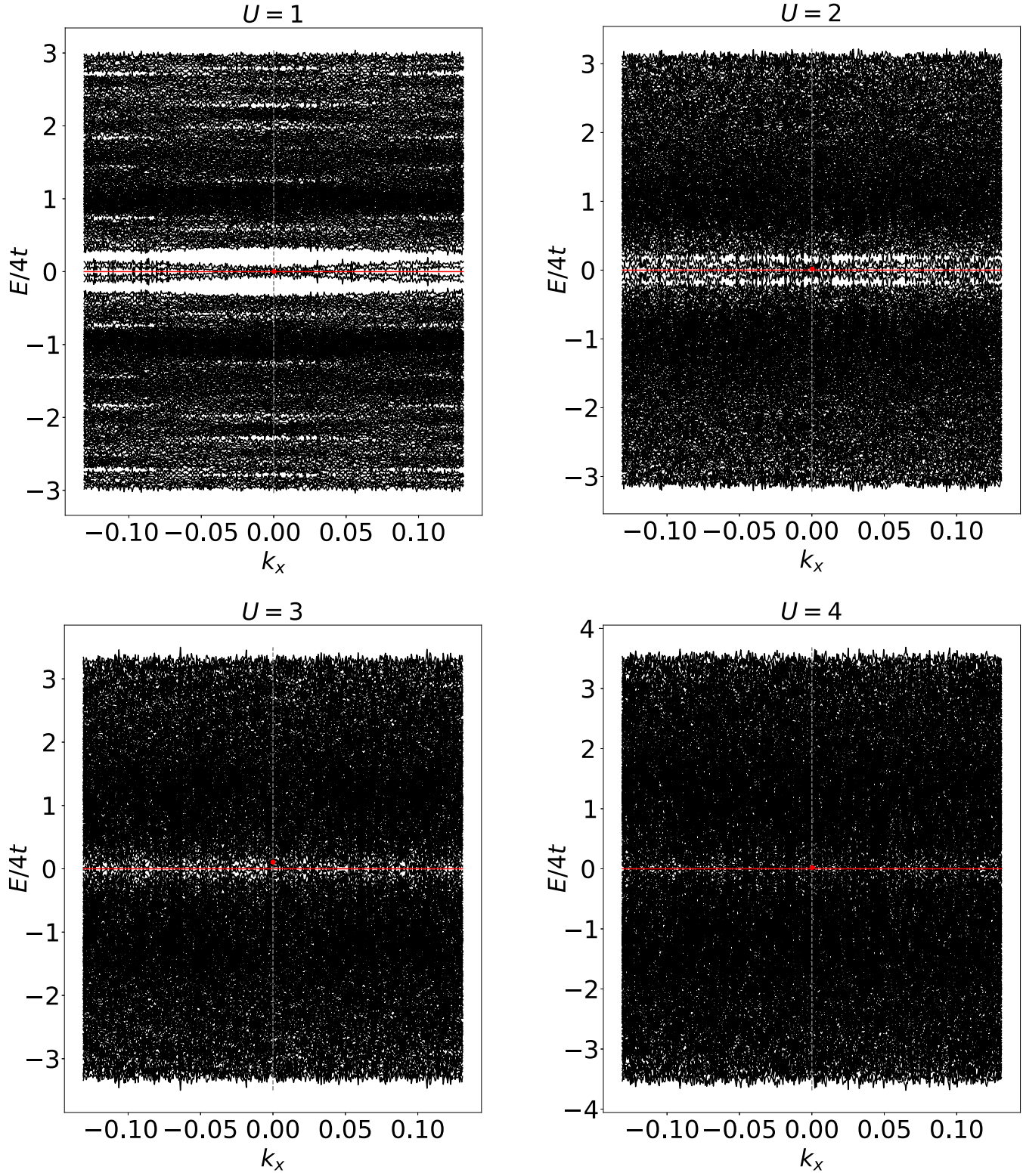

FIG. 14. Dispersion at the symmetric line limit using random configurations.

operator $a_k^\dagger$ is

$$a_k^\dagger = \frac{1}{N_u}\sum_{x_u,i} e^{-ik_x x_u} C_i^\kappa a_{x_u,i}^\dagger, \tag{A2}$$

where the sum is over N_u locations of the unit cells located at positions x_u and the ions i within each unit cell. The coefficients C_i^κ are the noninteracting eigenvector components obtained from the diagonalization of the tight-binding Hamiltonian. For the low-energy localized state, we have that $k_x = 0$

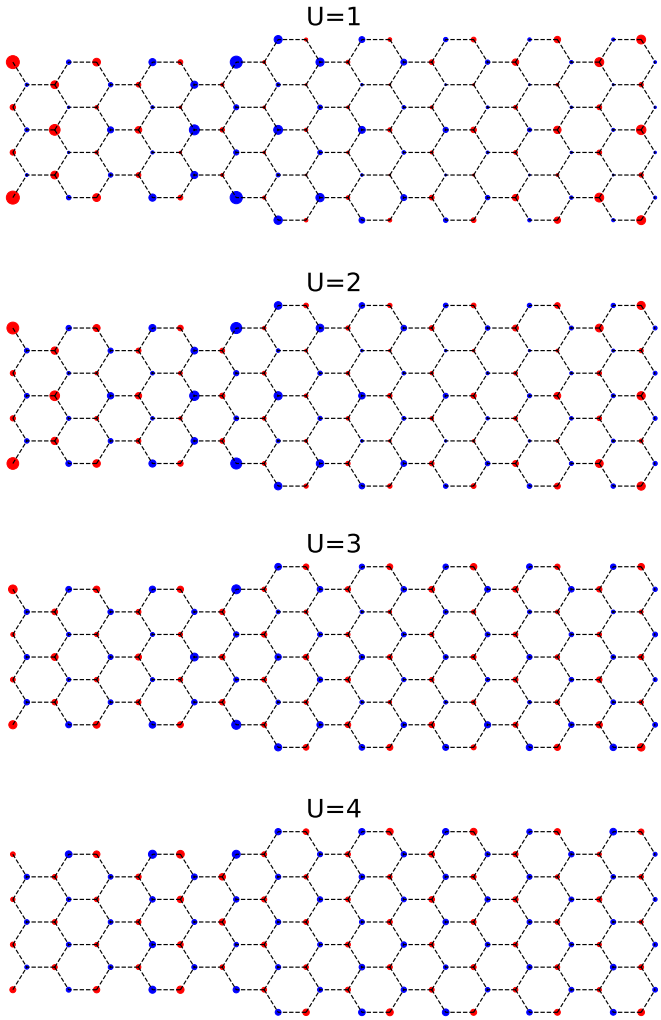

FIG. 15. Density profile of the lowest $k_x = 0$ energy state at the symmetric line limit using random configurations for different values of U. Localization can be seen in the cases with $U = 1$ and 2, but is lost for higher values.

and choose κ to correspond to the (noninteracting) eigenvector corresponding to this localized state.

By expressing the time dependence on the right-hand side of Eq. (A1) in the Heisenberg picture,

$$a_x(t) = e^{-Ht} a_x e^{Ht} ,$$

we can perform a spectral decomposition and determine the leading dependence of this correlator in the large time limit. We find

$$\lim_{1 \ll t < \beta} C_k(x,t) = \langle \Omega | a_x | \Omega + k \rangle \langle \Omega + k | a_k^\dagger | \Omega \rangle e^{-(\varepsilon_{\Omega+k} - \varepsilon_\Omega)t} + \ldots , \tag{A3}$$

where the ellipsis represents terms that are exponentially suppressed. The state $|\Omega\rangle$ and its associated energy ε_Ω represents the half-filling global ground state and global interacting energy minimum, respectively, and the state $|\Omega + k\rangle$ and associated energy $\varepsilon_{\Omega+k}$ is the state with an additional fermion with momentum k above half filling and its corresponding interacting energy, respectively. The energy *difference*

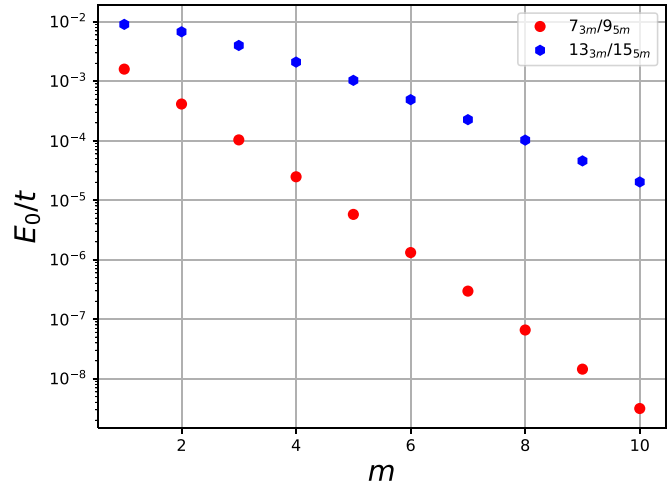

FIG. 16. The noninteracting energy of the localized state for both 7/9 and 13/15 ribbons as the bulk direction between junctions is extended in multiples of m. The width between the junctions is $3m$ ($5m$) for the lesser (greater) ribbon, corresponding $6m$ ($10m$) hexagonal units. When $m = 1$, we have the unit cells depicted in Fig. 1.

$\varepsilon_{\Omega+k} - \varepsilon_\Omega \equiv E_k$ is exactly the interacting energy that we refer to in the main text.

The amplitude we are interested in is $\langle \Omega | a_x | \Omega + k \rangle$. Note that in the noninteracting limit, we have that $\langle \Omega + k | a_k^\dagger | \Omega \rangle = 1$ and the amplitude is, up to an overall phase, equivalent to C_i^κ in Eq. (A2). With interactions, unfortunately, we cannot extract this amplitude because it is multiplied by the factor $\langle \Omega + k | a_k^\dagger | \Omega \rangle e^{-(E_{\Omega+k} - E_\Omega)t}$ which we do not *a priori* know. However, note that this factor is *independent* of site x

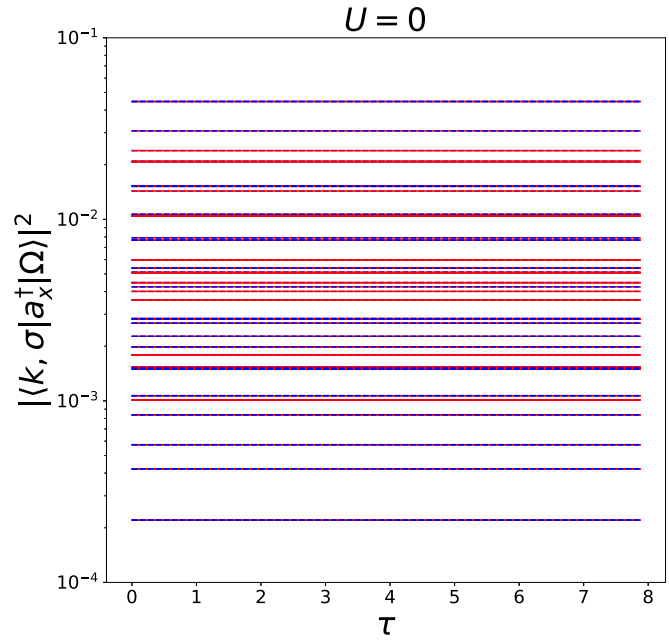

FIG. 17. Noninteracting wave-function densities $\rho_k(x,t)$ (labeled as $|\langle k, \sigma | a_x^\dagger | \Omega \rangle|^2$ above) of the lowest energy localized state, as defined by Eq. (A4). The different lines correspond to different lattice sites x and the red/blue coloring refer to A/B sites.

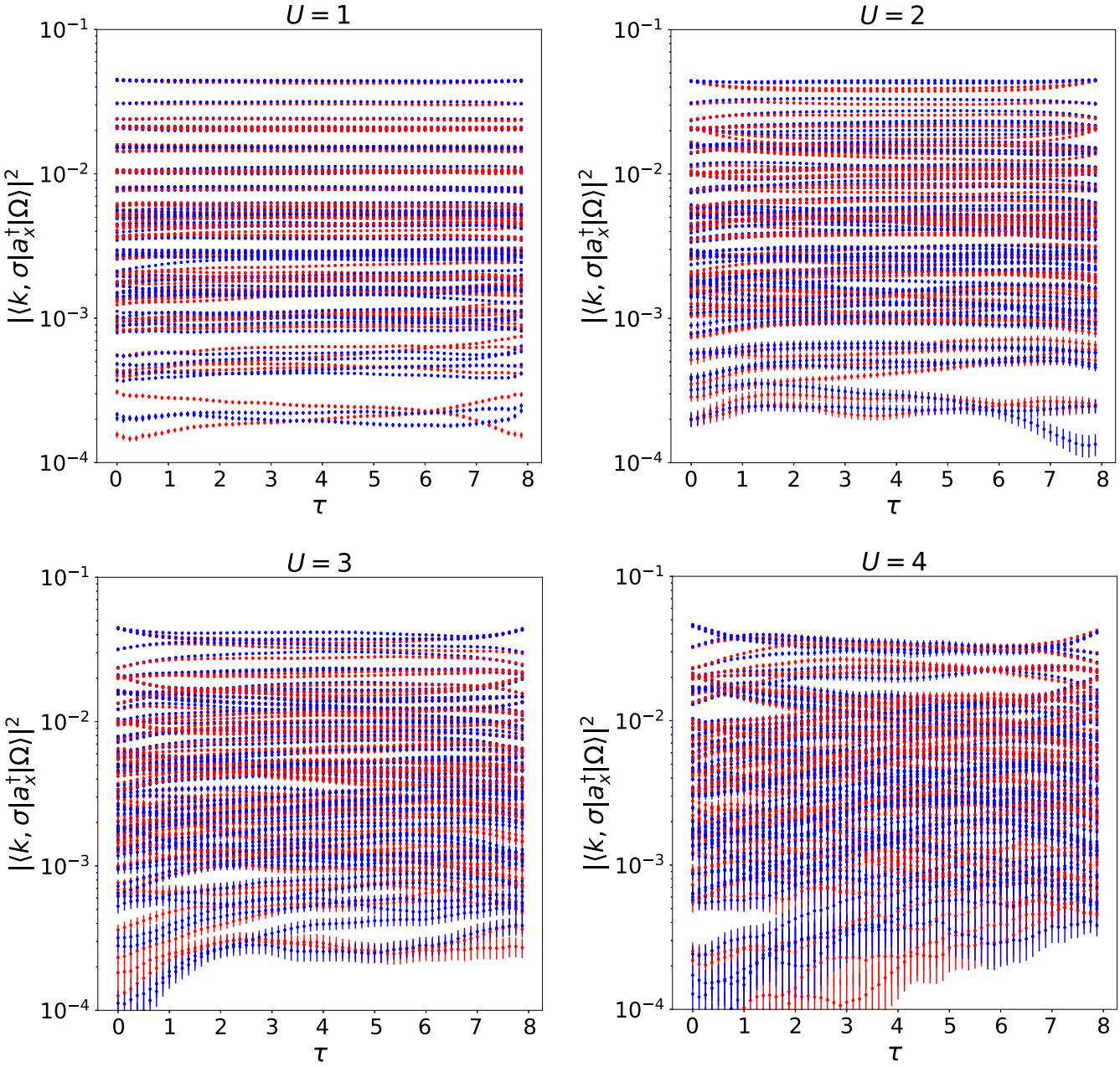

FIG. 18. Same as is in Fig. 17, but now with nonzero values U. The noninteracting amplitudes at $U = 0$ are shown in Fig. 17.

and carries the same time dependence for all spatial correlators. Furthermore, we are interested in the densities, $\rho_k(x) = |\langle\Omega|a_x|\Omega + k\rangle|^2$ which should be normalized over the lattice unit cell, $\sum_x \rho_k(x) = 1$. With these properties in mind, we instead analyze the following expression:

$$\rho_k(x,\tau) \equiv \frac{|C_k(x,\tau)|^2}{\sum_y |C_k(y,\tau)|^2}. \tag{A4}$$

Because of the independence of the unknown factor on spatial site x and its identical time dependence for each spatial site, this factor cancels in this ratio. The resulting term is automatically normalized over all lattice sites and thus represents the density at each site x. In the noninteracting limit, the cancellation of the unknown factor occurs exactly for all τ, and so Eq. (A4) has no dependence on τ. We have verified that it produces the exact wave-function densities, as shown in Fig. 17. For $U \neq 0$, the cancellation of the unknown factor occurs only in the scaling region given in Eq. (A3), and so we extract the densities in the region where $\rho_k(x,t)$ exhibits little to no time dependence and is thus relatively flat. Figure 18 shows examples of the $\rho_k(x,t)$ for different values of U, including the noninteracting case. In all cases, we extract the density in a region centered around $t = \beta/2$.

[1] T. Cao, F. Zhao, and S. G. Louie, Topological Phases in Graphene Nanoribbons: Junction States, Spin Centers, and Quantum Spin Chains, Phys. Rev. Lett. **119**, 076401 (2017).

[2] D. J. Rizzo, G. Veber, T. Cao, C. Bronner, T. Chen, F. Zhao, H. Rodriguez, S. G. Louie, M. F. Crommie, and F. R. Fischer, Topological band engineering of graphene nanoribbons, Nature (London) **560**, 204 (2018).

[3] O. Gröning, S. Wang, X. Yao, C. A. Pignedoli, G. Borin Barin, C. Daniels, A. Cupo, V. Meunier, X. Feng, A. Narita, K. Müllen, P. Ruffieux, and R. Fasel, Engineering of robust topological quantum phases in graphene nanoribbons, Nature (London) **560**, 209 (2018).

[4] D. J. Rizzo, J. Jiang, D. Joshi, G. Veber, C. Bronner, R. A. Durr, P. H. Jacobse, T. Cao, A. Kalayjian, H. Rodriguez, P. Butler, T. Chen, S. G. Louie, F. R. Fischer, and M. F. Crommie, Rationally designed topological quantum dots in bottom-up graphene nanoribbons, ACS Nano **15**, 20633 (2021).

[5] K. Wakabayashi, Ken-ichi Sasaki, T. Nakanishi, and T. Enoki, Electronic states of graphene nanoribbons and analytical solutions, Sci. Tech. Adv. Mater. **11**, 054504 (2010).

[6] M. Ezawa, Exact solutions for two-dimensional topological superconductors: Hubbard interaction induced spontaneous symmetry breaking, Phys. Rev. B **97**, 241113(R) (2018).

[7] S. R. Eric Yang, M.-C. Cha, H. J. Lee, and Y. H. Kim, Topologically ordered zigzag nanoribbon: $e/2$ fractional edge charge, spin-charge separation, and ground state degeneracy, Phys. Rev. Res. **2**, 033109 (2020).

[8] J.-J. Miao, D.-H. Xu, L. Zhang, and F.-C. Zhang, Exact solution to the Haldane-BCS-Hubbard model along the symmetric lines: Interaction-induced topological phase transition, Phys. Rev. B **99**, 245154 (2019).

[9] D. B. Kaplan, A Method for simulating chiral fermions on the lattice, Phys. Lett. B **288**, 342 (1992).

[10] Y. Shamir, Chiral fermions from lattice boundaries, Nucl. Phys. B **406**, 90 (1993).

[11] J.-W. Rhim, J. Behrends, and J. H. Bardarson, Bulk-boundary correspondence from the intercellular Zak phase, Phys. Rev. B **95**, 035421 (2017).

[12] R. Kundu, Tight binding parameters for graphene, Mod. Phys. Lett. B **25**, 163 (2011).

[13] T. Luu and T. A. Lähde, Quantum Monte Carlo calculations for carbon nanotubes, Phys. Rev. B **93**, 155106 (2016).

[14] J. Ostmeyer, E. Berkowitz, S. Krieg, T. A. Lähde, T. Luu, and C. Urbach, Semimetal–Mott insulator quantum phase transition of the Hubbard model on the honeycomb lattice, Phys. Rev. B **102**, 245105 (2020).

[15] J. Ostmeyer, E. Berkowitz, S. Krieg, T. A. Lähde, T. Luu, and C. Urbach, Antiferromagnetic character of the quantum phase transition in the Hubbard model on the honeycomb lattice, Phys. Rev. B **104**, 155142 (2021).

[16] N. N. Bogolyubov, On a New method in the theory of superconductivity, Nuovo Cim. **7**, 794 (1958).

[17] J. G. Valatin, Comments on the theory of superconductivity, Nuovo Cim. **7**, 843 (1958).

[18] H. B. Nielsen and M. Ninomiya, No Go Theorem for Regularizing Chiral Fermions, Phys. Lett. B **105**, 219 (1981).

[19] C. Gattringer and C. B. Lang, Lect. Notes Phys. **788**, 1 (2010).

[20] Z. Chen, X. Li, and T. Ng, Exactly Solvable BCS-Hubbard Model in Arbitrary Dimensions, Phys. Rev. Lett. **120**, 046401 (2018).

[21] G. Semenoff, Condensed Matter Simulation of a Three-Dimensional Anomaly, Phys. Rev. Lett. **53**, 2449 (1984).

[22] G. Semenoff, Chiral symmetry breaking in graphene, Phys. Scr. **T146**, 014016 (2012).

[23] B. Bernevig and T. Hughes, *Topological Insulators and Topological Superconductors* (Princeton University Press, New Jersey, 2013).

[24] T. Stanescu, *Introduction to Topological Quantum Matter & Quantum Computation* (CRC Press, Taylor & Francis Group, Florida, 2017).

[25] D. Smith and L. Smekal, Monte-Carlo simulation of the tight-binding model of graphene with partially screened Coulomb interactions, Phys. Rev. B **89**, 195429 (2014).